Spectroscopic Imaging of Strongly Correlated Electronic States

Ali Yazdani,[1] Eduardo H. da Silva Neto,[2,3] and Pegor Aynajian[4]

[1]Joseph Henry Laboratories and Department of Physics, Princeton University, Princeton, New Jersey 08544; email: yazdani@princeton.edu

[2]Department of Physics & Astronomy, University of British Columbia, Vancouver, British Columbia V6T 1Z1, Canada; email: ehda@physics.ubc.ca

[3]Quantum Materials Program, Canadian Institute for Advanced Research, Toronto, Ontario M5G 1Z8, Canada

[4]Department of Physics, Applied Physics and Astronomy, Binghamton University, Binghamton, New York 13902; email: aynajian@binghamton.edu

Annu. Rev. Condens. Matter Phys. 2016. 7:11–33

First published online as a Review in Advance on January 7, 2016

The *Annual Review of Condensed Matter Physics* is online at conmatphys.annualreviews.org

This article's doi: 10.1146/annurev-conmatphys-031214-014529

Keywords

scanning tunneling microscopy (STM), cuprates, heavy fermions, superconductivity

Abstract

The study of correlated electronic systems from high-T_c cuprates to heavy-fermion systems continues to motivate the development of experimental tools to probe electronic phenomena in new ways and with increasing precision. In the past two decades, spectroscopic imaging with scanning tunneling microscopy has emerged as a powerful experimental technique. The combination of high energy and spatial resolutions provided by this technique reveals unprecedented detail of the electronic properties of strongly correlated metals and superconductors. This review examines specific experiments, theoretical concepts, and measurement methods that have established the application of these techniques to correlated materials. A wide range of applications, such as the study of collective responses to single atomic impurities, the characterization of quasiparticle-like excitations through their interference, and the identification of competing electronic phases using spectroscopic imaging, are discussed.

1. INTRODUCTION

Understanding many-body correlations beyond those found in simple metals and semiconductors has been one of the most stimulating themes of recent research in condensed matter physics. The search for an appropriate theoretical description, likely beyond those based on Landau's quasiparticle excitations of a Fermi liquid, as well as a detailed understanding of the mechanism of superconductivity in correlated systems is benefiting from the development of new experimental techniques. In the past two decades, the scanning tunneling microscope (STM) has become a powerful tool for studying electronic phenomena with increasing numbers of applications to correlated systems. High-energy resolution spectroscopy and spectroscopic imaging with the STM provide a wealth of electronic information and is becoming as common an experimental tool as angle-resolved photoemission spectroscopy (ARPES) for characterizing novel electronic materials. This review illustrates how STM has been used to probe correlated electronic phenomena in a variety of materials and describes the utility of this technique for future studies of these materials.

Electron tunneling spectroscopy in metals, semiconductors, and superconductors has a long history of important discoveries in condensed matter physics. The technique was launched by Giaever's first direct measurement of the superconducting energy gap in the quasiparticle density of states (DOS) as predicted by Bardeen-Cooper-Schrieffer (BCS) for conventional superconductors (1). A subsequent breakthrough was achieved by McMillan & Rowell who showed that electron-phonon coupling gives rise to distinct features in the tunneling spectra; they provided an experimental confirmation for the electron-phonon mechanism of conventional superconductors through an analysis based on Eliashberg's strong-coupling theory (2). Following these initial discoveries, tunneling spectroscopy has proven to be an important technique for condensed matter experimentalists.

With the invention of the STM by Binnig & Rohrer came the expectation that tunneling spectroscopy would be considerably advanced. Spatially resolved tunneling spectra can be obtained by using the STM and enables the correlation of this local electronic information with simultaneously measured atomic-scale images (3). Given that the energy resolution of tunneling spectroscopy is ultimately determined by the Fermi occupation and, hence, by the temperature of the tip and the sample, development of cryogenic STM instrumentation in the past two decades has resulted in novel applications for this technique.

Low temperature operation also made atomic manipulation possible, capturing the public's imagination by creating quantum corrals (4). The quantum corrals provided an early test of STM's ability to obtain precise spectroscopic information about quasiparticle excitations of a simple electronic system that could be theoretically computed (5). Moving beyond simple metals, application of STM to probe local correlations in the vicinity of individual magnetic defects in metals and BCS superconductors provided another early example of the STM applicability to the study of local correlated phenomena (6, 7). Following work on spectroscopic imaging of surface electrons, the Fourier transform of these maps was recognized to contain information about the Fermi surface through quasiparticle scattering interference (8). Access to the energy-momentum dispersion of these quasiparticle states through their interference patterns—both below and above the Fermi level—has made spectroscopic imaging with the STM (SI-STM) an important complementary technique to ARPES. At other times, STM spectroscopy has also been an important complementary tool to scattering experiments such as those utilizing X-rays to probe charge ordering phenomena. Given the propensity of correlated systems to have many competing phases, the ability of STM to correlate spectroscopic information with ordering phenomena at the atomic scale is increasingly important.

The outline of this review is as follows. We briefly describe in Section 2 the basic principle and theory behind the operation of STM and spectroscopic imaging, including some discussion of instrumental requirements for high-resolution measurements. Starting with experiments on single impurities in simple metals and conventional superconductors, we describe in Section 3 how SI-STM can obtain signatures of local correlation in these systems that can be directly compared with theoretical calculations. In Section 4, we discuss the application of STM to high-T_c cuprate superconductors, which is perhaps the most widely recognized use of this technique; the continued refinement of this application has led to a number of important discoveries. The SI-STM technique is also starting to be successfully applied to other correlated systems, such as heavy-fermion compounds and Fe-based superconductors. However, studies of the latter significantly overlap with the cuprates, in both methodology and technical requirements, and have therefore been omitted [we recommend a recent review by Hoffman et al. (9)]. In Section 5, we review the recent developments in the study of heavy-fermion compounds and their unconventional metallic and superconducting states. Measurements of these Kondo systems highlight the importance of the tunneling matrix element, which can be used to sensitively probe the different components of composite quasiparticles. The studies of heavy-fermion superconductivity also provide the first successful applications of SI-STM at milli-Kelvin temperatures, opening the way for future experiments at these extreme temperatures. In Section 6, we briefly discuss ongoing applications of STM to other correlated electron systems. We close in Section 7 with an outlook of how the development of new experimental approaches may enhance the use of STM even further in the study of correlated electron systems.

2. LOCAL SPECTROSCOPY AND SPECTROSCOPIC IMAGING WITH THE SCANNING TUNNELING MICROSCOPE

The basic principle of STM operation relies on bringing a sharp metallic tip near (typically 5–6 Å) the sample such that electrons can tunnel between the two (see **Figure 1**). Scanning the tip across the surface and adjusting its height with a feedback loop to maintain a constant tunneling current (I_0) at a tip-sample bias V_0 constrains the tip to follow contours of constant electron density. The recorded height variation along the tip trajectory forms the STM topographic image, which is determined by the energy integration of the local density of states (LDOS) of the sample between the Fermi level and V_0, providing both electronic and structural information. To perform atomic-resolution images, the tip must be sharp and close enough to the surface to resolve the spatial variation of the LDOS. Tunneling spectroscopy with the STM is performed by recording the differential conductance between the tip and the sample, at a fixed tip location and height relative to the sample, as a function of V_0. To obtain reproducible spectra it is critical that the sample surface is prepared in situ through sputtering/annealing cycles or by cleaving, and studied under ultrahigh vacuum conditions. The temperature of the tip and sample, the relative motion of the tip with respect to the sample, and the electrical noise associated with either V_0 or the current measurements all contribute in determining the resolution of such local spectroscopic measurements. It is therefore desirable to use STM instruments that operate at low temperatures—in ultraquiet, seismically isolated and acoustic environments—together with sufficient electrical filtering and radio frequency shielding.

In general, the measured current and the differential conductance depend on the LDOS of the sample N_S and tip N_T, the convolution of their Fermi functions f, and the matrix element for the tunneling process M (10):

$$I(eV) = \frac{4\pi e}{\hbar} \int [f(E_F - eV + E) - f(E_F + E)]|M|^2 N_T(E_F + E) N_S(E_F - eV + E) dE. \quad 1.$$

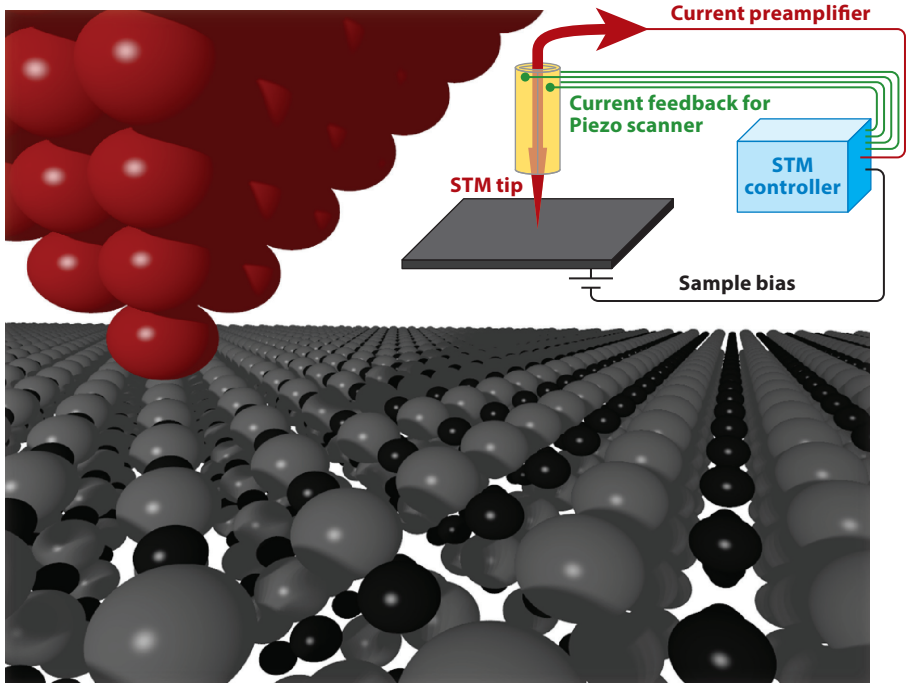

Figure 1

Schematic diagram of a scanning tunneling microscope (STM).

Typically, high-resolution tunneling spectroscopy is focused on electronic states near the Fermi energy; for this narrow energy window, N_T and $|M|^2$ can often be assumed to have negligible energy dependence. Then in the low-temperature limit, the dI/dV measurements as a function of energy are directly proportional to the sample's LDOS (11):

$$\frac{\mathrm{d}I}{\mathrm{d}V}(eV) \propto N_S(E_F - eV). \qquad 2.$$

However, there are still instances where either the tip's electronic structure or its geometry can strongly influence what is being measured in an STM conductance map—e.g., when probing rotational symmetry breaking (12) or in spin-polarized measurements (13). An experimental test that demonstrates how STM can match the sensitivity of planar tunneling spectroscopy experiments is to use STM to probe the electronic properties of a conventional BCS superconductor. As shown in **Figure 2** for a Pb single crystal, STM spectroscopy can recover not only the BCS DOS and the superconducting gap but also signatures of electron-boson coupling outside the gap.

SI-STM is performed by recording dI/dV as a function of V on a set of predetermined points on a line or grid. These measurements are the most demanding in terms of stability of the STM instrument as this determines the signal-to-noise ratio and the time required for averaging at each location. STM spectroscopy studies over the past two decades have shown consistent improvement in the size and energy resolution of these maps as instrumentation is built with lower background noise. The cryogenic instruments that make these kinds of measurements possible are ultimately limited by the hold time of the He cryostat, which sets the upper limit for the total time available

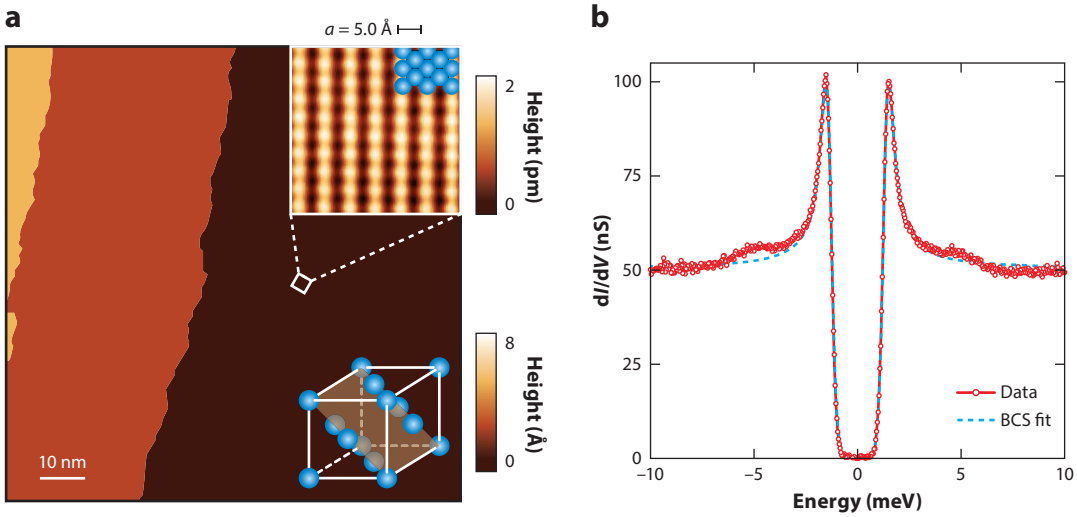

Figure 2

(*a*) Scanning tunneling microscope (STM) topography of Pb(110) surface shows atomic ordered terraces. Inset shows an atomic-resolution image of the underlying lattice. (*b*) STM tunneling spectra (*red line*) measured on the surface shown in panel *a* together with a fit to a Dynes function (with gap value $\Delta = 1.35$ meV at 1.46 K). The features at energies outside the gap are the result of electron-phonon coupling. Abbreviation: BCS, Bardeen-Cooper-Schrieffer.

for each run and the averaging time at each pixel of the spectroscopic image. It is not unusual for such high-resolution spectroscopic maps to require several days to complete.

In the absence of any imperfection on the sample surface, when translational symmetry is preserved, spectroscopic imaging measurements would be spatially uniform and, therefore, offer no more information than the point spectra. However, the introduction of a small concentration of defects, often already present even in the cleanest materials (e.g., adatoms or atomic steps), gives rise to scattering of quasiparticle excitations and quasiparticle interference (QPI). In this case the local symmetries are broken, and the spectroscopic images at a specific energy display spatial modulations of the LDOS as a result of this interference. These modulations occur at a wave vector $\mathbf{Q} = \mathbf{K}_f - \mathbf{K}_i$, where $\mathbf{K}_i$ and $\mathbf{K}_f$ are the momenta of the initial and final states, respectively, of scattering processes that occur on the contours of constant energy. **Figure 3*a–c*** shows examples of QPI between Cu(111) surface states at different voltages (B. Zhou, S. Misra, A. Yazdani, unpublished results). Their corresponding Fourier transforms (**Figure 3*d–f***) are circles whose radii vary as a function of energy, which can then be used to obtain the energy-momentum dispersion of the bands responsible for such scattering (**Figure 3*g***). The interpretation of QPI measurements requires some initial assumptions—usually from ARPES or band structure calculations—regarding the topology of the band structure of the material and its projection onto the surface where the measurements are being performed. However, QPI measurements complement ARPES studies because they can be carried out with higher energy-resolution (at low enough temperature) and with sufficient resolution in momenta (provided sufficiently large areas of the sample are measured). Furthermore, unlike ARPES, QPI measurements can probe both occupied and unoccupied states, which can be an important asset in the study of particle-hole asymmetric excitations in superconductors.

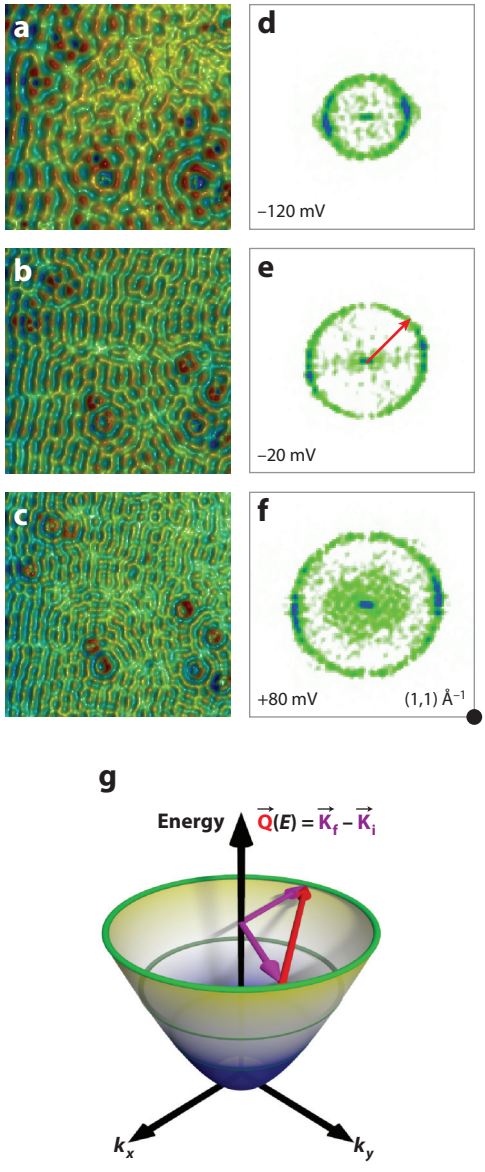

Figure 3

Scanning tunneling microscope conductance maps (*a–c*) and their Fourier transforms (*d–f*) at the corresponding energies of Cu(111) surface states. (*g*) Schematic band structure of the surface state and the elastic scattering between initial and final momentum states ($\mathbf{K_f} - \mathbf{K_i}$) that give rise to interference $\mathbf{Q}$ that appears in the Fourier transform of the conductance maps.

3. LOCAL CORRELATED PHENOMENA: MAGNETIC IMPURITIES IN METALS AND SUPERCONDUCTORS

One of the earliest examples of correlated electronic phenomena in solids is the Kondo effect, which gives rise to a resistance minimum in metals that have a small concentration of magnetic impurities (14). The key signature of the Kondo state is a sharp resonance in the DOS at the

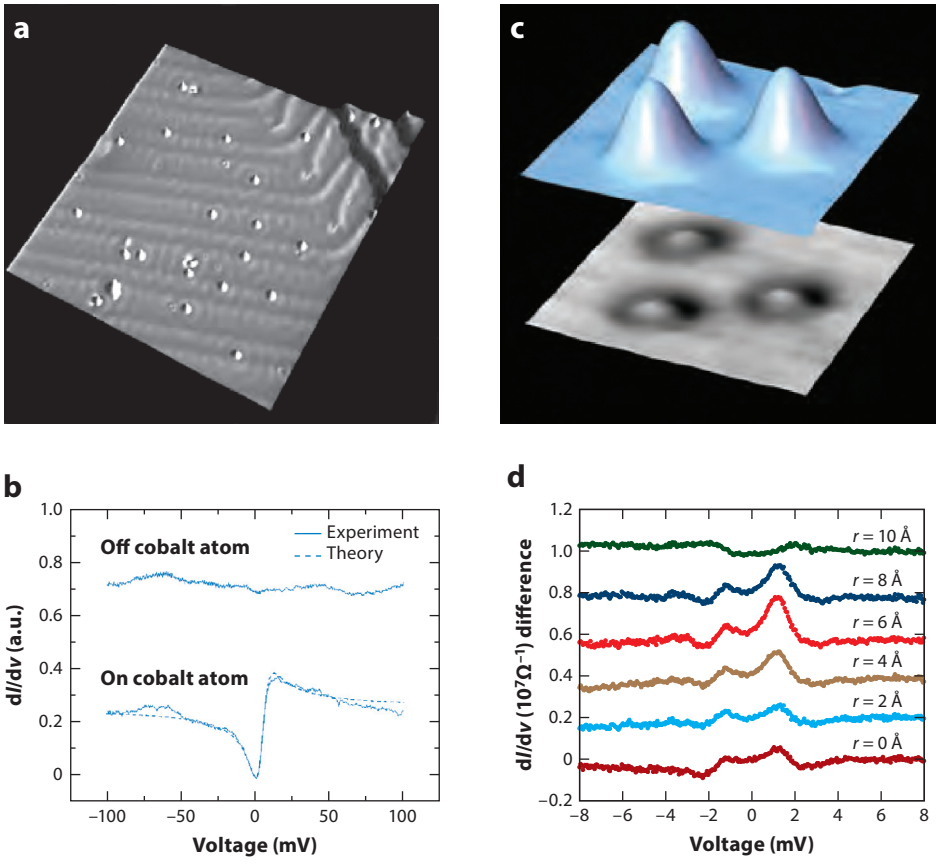

Figure 4

(*a*) STM image of single Co atoms on Au(111) surface. (*b*) Spectra on and off the individual atoms showing the Fano resonance associated with the Kondo effect (adapted with permission from Reference 7.) (*c*) Three Gd adatoms on Nb(110) surface. (*d*) STM spectra with the Bardeen-Cooper-Schrieffer (measured on the substrate) density of states subtracted to show the in-gap Shiba states associated with exchange scattering from the Gd atoms. Adapted with permission from Reference 6. Abbreviation: STM, scanning tunneling microscope.

Fermi level with a width determined by the Kondo temperature (T_K) (15). STM experiments on individual magnetic adatoms deposited on the surface of metals have provided a local examination of the Kondo resonance (7). Measurements of the tunneling spectrum in the vicinity of single magnetic impurities on a metal surface showed that the spectrum followed an asymmetric Fano line shape (**Figure 4*a*,*b***) instead of a resonant peak near the Fermi energy—a fact that highlights the importance of understanding the role of the tunneling matrix element M when measuring dI/dV. In this particular case tunneling can involve two processes: one in which electrons tunnel through the Kondo resonance to the continuum of states of the metal, and the other in which electrons tunnel directly into the continuum state. Interference between these two paths can then change the shape of the tunneling spectra to that of the experimentally observed Fano line shape. As discussed in Section 5, these results on single Kondo impurities are the basis for understanding STM measurements on heavy-fermion systems, which involve tunneling into composite quasiparticles.

STM measurements of magnetic defects on conventional superconductors were also used to probe the collective response of a BCS superconducting state to such impurities (6). It is well known that magnetic impurities are detrimental to superconductivity by suppressing the superconducting transition temperature. They had been predicted to enhance in-gap states due to the presence of impurity-induced Shiba states that emerge from the local exchange interaction between superconducting electrons and the spin of the magnetic impurity (16). Although there had been some evidence for such states from enhanced subgap conductance in magnetically doped superconducting planar junctions, STM experiments were the first to establish the presence of these localized states in the vicinity of single magnetic impurities and map their spatial structure (**Figure 4*c***). Solutions to the Bogoliubov-de Gennes (BdG) equations that describe the spatial anisotropy and extent of a superconductor's DOS near impurities were successfully used to describe the experimental results. In fact, two surprising aspects of these measurements were that the strength of the in-gap states rapidly decayed on the length scale of the Fermi wavelength and that the spectra displayed an asymmetry for tunneling between the electron and hole components of the bound state (**Figure 4*d***). Both of these features are successfully captured in the solutions of the BdG equations by adjusting the strength of the local magnetic and nonmagnetic coupling to the impurity atom (6, 17). These initial measurements and their modeling have been extended to understand similar phenomena related to the local response of unconventional superconductors to impurities.

4. SPECTROSCOPIC IMAGING OF HIGH-T_c SUPERCONDUCTORS

High-T_c cuprate superconductors have been the most studied, strongly correlated material systems for at least the past two decades (18, 19). Both the mechanism of unconventional *d*-wave pairing and the process by which doping transforms an antiferromagnetic Mott insulator into a correlated conductor are still highly debated. Much of the research focus has been on the hole-doped cuprates, which in addition to superconductivity and antiferromagnetism exhibit a pseudogap phase in underdoped samples characterized by a partially gapped Fermi surface (20). Within the pseudogap phase there is experimental evidence for short-range charge ordering (21), rotational symmetry breaking (22, 23), fluctuating superconductivity above T_c (24), and signatures of magnetic ordering in the form of orbital currents (25). Understanding the pseudogap phase and its connection to various forms of fluctuating order and superconductivity has been a central theme in cuprate research to which STM studies have contributed significantly (26).

Early spectroscopic measurement of the cuprates that provided support for the anisotropic *d*-wave superconducting gap came from ARPES studies of $Bi_2Sr_2CaCu_2O_{8+x}$ samples (27). ARPES measurements above T_c were also used to visualize the anisotropic structure of the pseudogap in momentum space and to establish the so-called Fermi arc in underdoped samples (28). The layered structure of Bi-based cuprates makes it possible to easily prepare atomically clean surfaces by cleaving, which not only led to the success of ARPES studies in cuprates but also made high-resolution STM experiments possible. Although there have been STM studies on other cuprates, they have not contributed as much to our understanding of these materials as the large body of STM work on $Bi_2Sr_2CaCu_2O_{8+x}$. Here we focus on three of the most influential STM contributions to our understanding of the cuprates. In Section 4.1, we address the spatially inhomogeneous nature of the local electronic states and relationship to the pseudogap in underdoped hole-doped cuprates. In Section 4.2, we discuss QPI measurements that probe the energy-momentum structure of the electronic excitations below and above the Fermi energy. Finally, in Section 4.3, we present the STM observation of a low-energy charge order competing with superconductivity.

4.1. From Local Dopants to Inhomogeneous Pairing

Atomic-resolution spectroscopic imaging of high-T_c cuprates began with studies of the effects of nonmagnetic defects on *d*-wave superconductivity (29, 30). Experiments on $Bi_2Sr_2CaCu_2O_{8+x}$ samples with natural and intentionally introduced defects showed that the *d*-wave-gap DOS was modified by the presence of low-energy Shiba-like excitations in the immediate vicinity of these defects. These results were followed by experiments that imaged the anisotropic clover-leaf shape of the impurity-induced state (17, 31–33). Moreover, SI-STM near crystallographic step edges oriented at 45° to the Cu-O bond direction also provided evidence for *d*-wave superconductivity via the observation of a one-dimensional Andreev bound state that originates from the scattering and interference of quasiparticles experiencing a π phase shift of the superconducting order parameter (34).

An important electronic property of the cuprates uncovered by STM studies is the strong spatial fluctuation of the LDOS at the nanometer scale (35–37). The LDOS and the apparent *d*-wave-like gap measured on $Bi_2Sr_2CaCu_2O_{8+x}$ show remarkable variations on length scales of 20–30 Å for all doping levels studied. Such local fluctuations appear to be a natural outcome of random doping of these Mott insulators. Analogous to studies in semiconductors, SI-STM at high bias has been used to identify the location of the dopants and to reveal their correlation with spatial fluctuations of the LDOS (38). The different dopants have different spectroscopic signatures; this is a complication that made the initial counting of dopants, and their correlation with the changes in the LDOS, confusing (38). However, recent progress in accounting for all the dopants indicated that apical oxygen vacancies appear to play a prominent role and directly impact the spatial inhomogeneity of the pseudogap electronic states of $Bi_2Sr_2CaCu_2O_{8+x}$ samples (39). Regardless of the role of the different types of dopants, they are likely to impact both normal and superconducting states.

Understanding the spatial correlation between the superconducting and normal states proved to be a greater challenge, demanding SI-STM measurements over a large temperature range and on the same subnanometer region. An experimental method that allowed the precise extraction of the effects of superconductivity on the LDOS was the development of lattice tracking spectroscopy with the STM (37, 40). By using specially designed STM instruments with minimal thermal drift, it is possible to track the changes in the tunneling spectra at an exact atomic location over nearly a 100-K temperature range and, consequently, measure the LDOS in the normal and superconducting states.

Several important aspects of the pairing gap in the cuprates have been uncovered in temperature-dependent STM studies of overdoped $Bi_2Sr_2CaCu_2O_{8+x}$ samples in which the pseudogap is absent. First, these measurements show that a *d*-wave pairing gap is present at temperatures T_p higher than the bulk T_c of the sample in nanoscale regions (**Figure 5*a*,*b***) (37, 40). The fits to the *d*-wave gaps show that though the magnitude of the gap is being suppressed with increasing temperature, it is the quasiparticle lifetime broadening that exhibits the most dramatic changes at the bulk T_c (**Figure 5*c***) (40). The persistence of the pairing gap above the bulk T_c has been confirmed by recent high-resolution ARPES studies that also show the enhanced lifetime broadening in the spectra above T_c (41). Another surprising discovery of these measurements is that the spatial variations of the pairing gap do not smooth out with increasing temperature (**Figure 5*a***). In fact, for a conventional BCS superconductor (even in the *d*-wave case), the expectation is that near T_c any spatial variations of the superconductor gap should disappear owing to a diverging superconducting coherence length. As pointed out earlier, spatial variations of the LDOS of the normal state appear to occur on the same length scale as the pairing gap variations, and the two are strongly correlated. These experiments also revealed that local fluctuations in the magnitude of the gap and the associated temperature, at which each gap closes at T_p, have a remarkably constant ratio, with small corrections caused by a short-range proximity effect (42).

Figure 5

(*a*) Lattice tracking spectroscopy measuring the gap maps taken on the same 300-Å area on an overdoped $Bi_2Sr_2CaCu_2O_{8+x}$ sample ($T_c = 65$ K) at different temperatures near T_c. Adapted with permission from Reference 37. (*b*) Extracted values of the pairing gap for several different locations are plotted as a function of temperature. The gray line indicates the resistive T_c. (*c*) Lifetime broadening at different temperatures is plotted as a function of the corresponding low-temperature gap. The inset of panel *c* shows how the average lifetime broadening continues to increase above T_c. Adapted with permission from Reference 40.

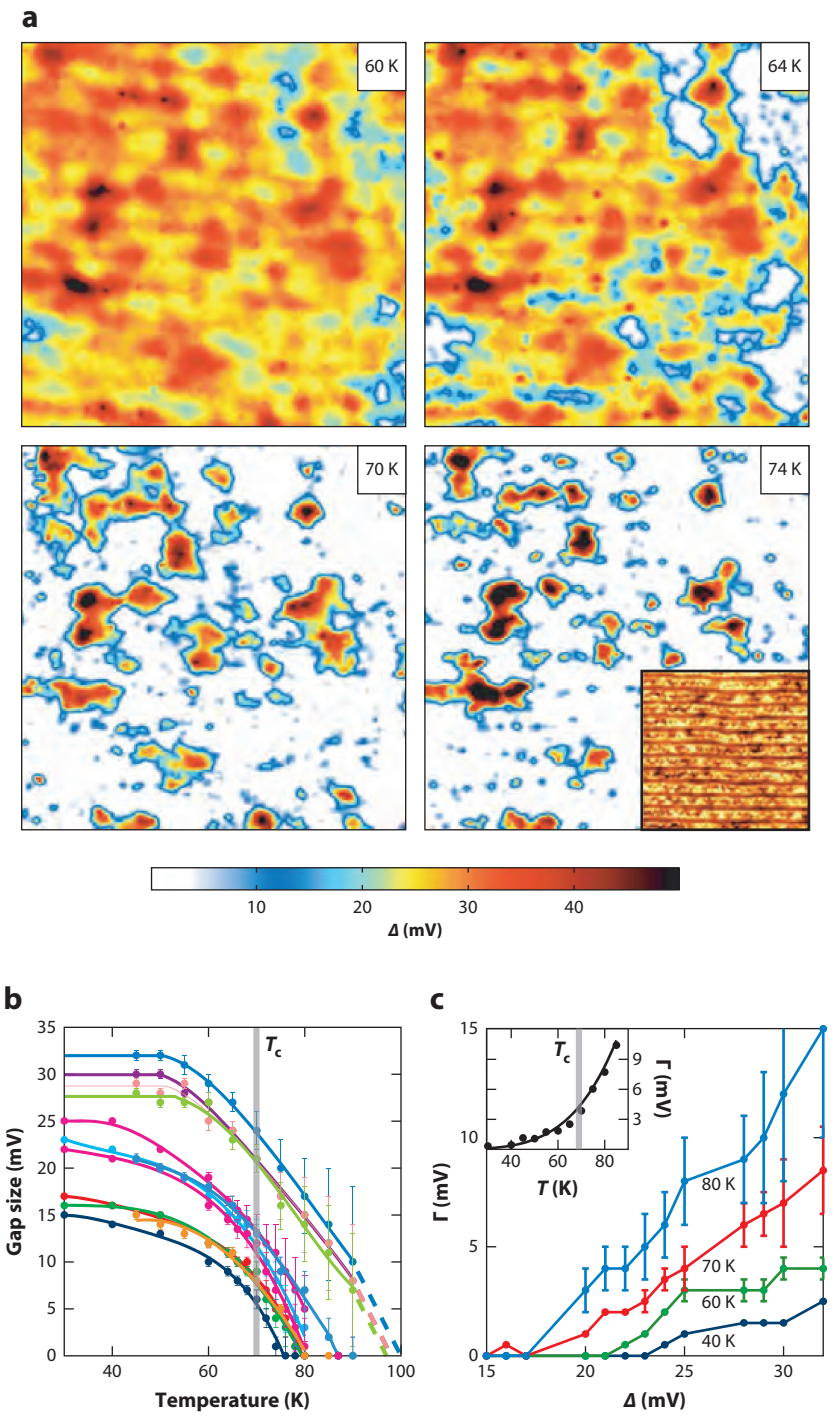

Finally, the lattice tracking technique made it possible to precisely study the electron-boson coupling features of the tunneling spectra that occur beyond the maximum *d*-wave gap energy. The ratios of these spectra, as in conventional planar tunnel junctions, were used to isolate the superconductivity-related features from the spatially inhomogeneous normal-state background (40). Such studies illustrated that though the electron-boson features that appear at energies higher than the maximum *d*-wave gap track the local variation of the gap, they do not change in magnitude in regions with different gaps. Such insensitivity to pairing gap variation suggests the boson responsible for these features (around 40 meV) is not playing the leading role in the pairing mechanism.

Overall, the formation of pairing above T_c in underdoped cuprates together with the earlier observation of diamagnetic response above T_c suggests that pairing in the cuprates is a highly local phenomenon. These measurements provide evidence that phase coherence rather than pair formation dominates the physics of the transition between the superconducting and resistive states (43, 44).

4.2. Energy-Momentum Structure of the Superconducting and Pseudogap Electronic States

One of the most successful applications of SI-STM to the high-T_c cuprates has been the measurement of QPI patterns and their relationship to the ARPES measured Fermi surface (45–47). In the superconducting state, spatial modulations of the dI/dV due to QPI originate from BdG quasiparticles that scatter from random weak impurities present in $Bi_2Sr_2CaCu_2O_{8+x}$ samples. The Fourier transforms of these patterns reveal a set of seven wave vectors that disperse as a function of energy. These wave vectors can be related to how superconductivity transforms the band structure into banana-shaped contours of constant energy situated on top of the underlying Fermi surface; this is the so-called octet model (**Figure 6*a*,*b***). Scattering dominated by the large DOS at the end of these banana-shaped contours provides a reasonable description (45) for the dispersion of these wave vectors for near-optimally doped and overdoped samples and correlates well with ARPES studies on similar samples. Although the interpretation of QPI studies on underdoped samples is still debated (see Section 4.3 below), for overdoped samples the QPI measurements are consistent with a single band (hole-like) and a *d*-wave gap as determined by ARPES measurements on similar samples (47). Indeed, recent QPI analysis of one of the octet wave vectors $\mathbf{q}_4$, which connects the extrema of the Fermi surface in Bi-2212, shows the Fermi surface to exhibit a single hole-like band in the overdoped regime, which changes to discrete arcs in the underdoped regime (**Figure 6*c***) (48; see also Reference 49 for a similar finding on single-layer Bi-2201).

In underdoped cuprates, signatures of deviation from a conventional *d*-wave superconductor can be seen in both the STM spectra (**Figure 7*a***) and the QPI analysis. In general, the spectra show a linear regime at low bias (below 20 meV) and a distinct break indicating the presence of a pseudogap energy scale at higher bias (50–100 meV) (**Figure 7*a*,*b***). Raising the temperature above T_c, the shape of the tunneling spectra shows a high-energy feature that persists up to the pseudogap temperature (T^*) far above T_c (**Figure 7*a***); this in in agreement with other spectroscopic techniques (28, 50). The presence of two separate energy scales at low temperatures in the tunneling spectra (51–53) becomes more evident with a decrease in the doping in Bi-based cuprates and has been corroborated by recent ARPES studies (54). The pseudogap energy scale is larger for more underdoped samples but merges with the superconducting gap near optimal doping (**Figure 7*b***).

One approach in understanding these different energy scales has been to model the STM spectra as a momentum-integrated probe of the DOS (53). At low bias, the spectra probe the

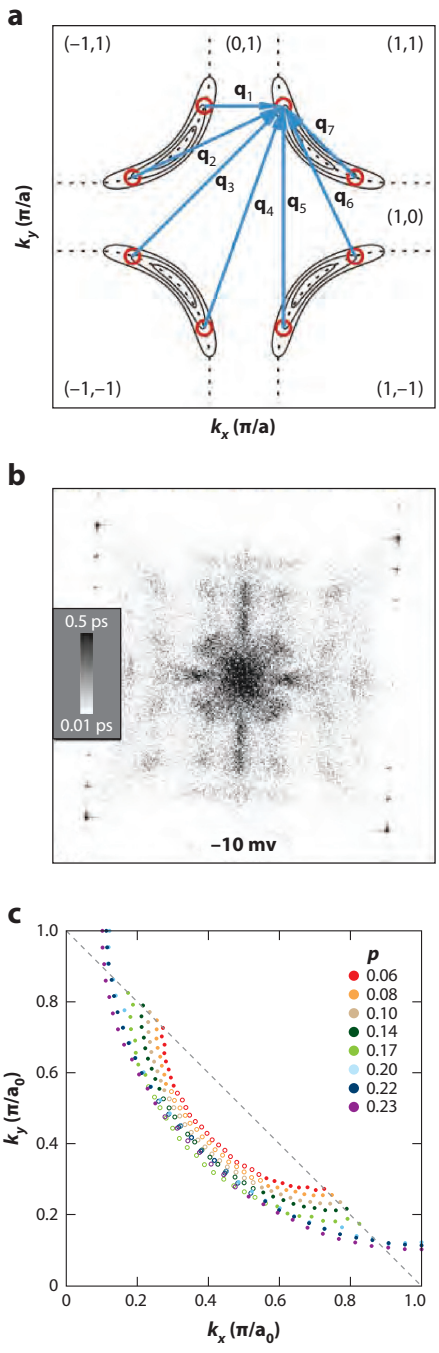

Figure 6

(*a*) Schematic of the $Bi_2Sr_2CaCu_2O_{8+x}$ band structure and its modification with the presence of a *d*-wave gap. The wave vectors $\mathbf{q_1}$–$\mathbf{q_7}$ connect points of high density of states and give rise to the quasiparticle interference signal measured in panel *b*. Adapted with permission from Reference 47. (*c*) Analysis of the $\mathbf{q_4}$ wave vector showing the transition from disconnected Fermi arcs to a closed Fermi surface as a function of doping. Adapted with permission from Reference 48.

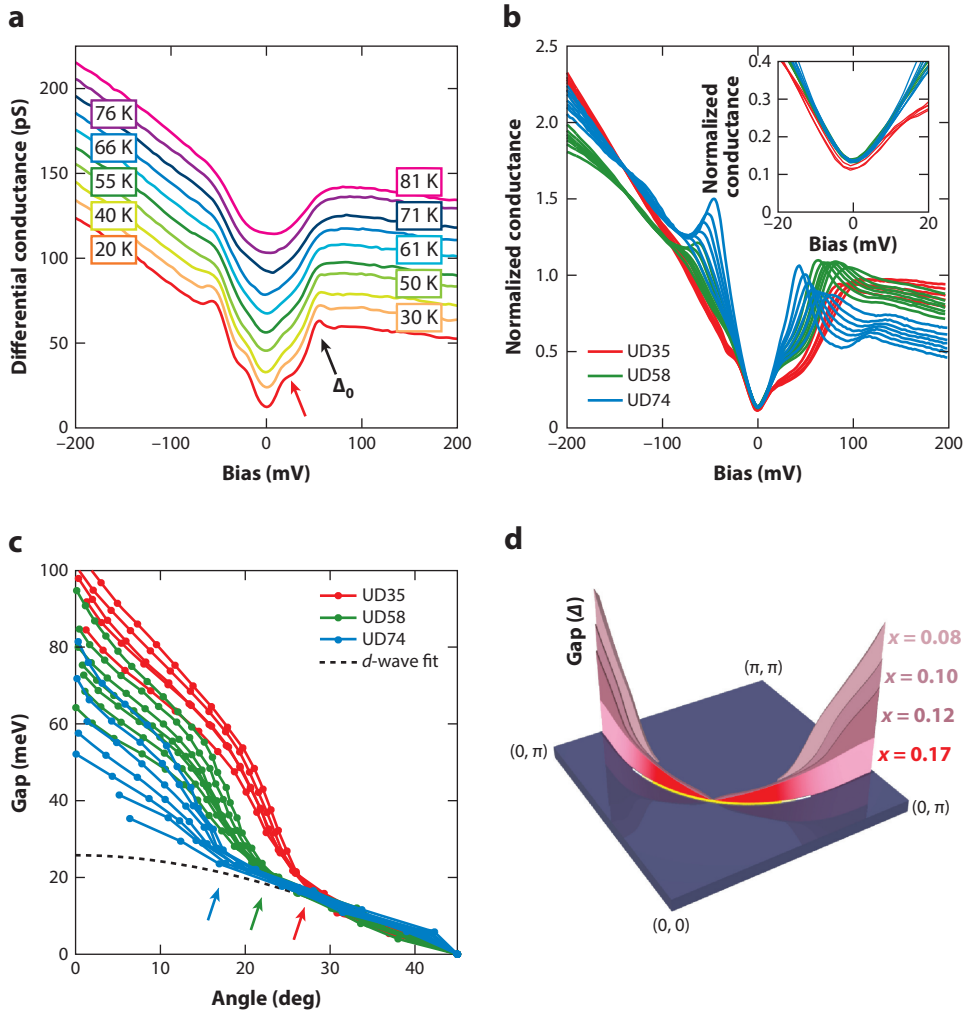

Figure 7

(*a*) Lattice tracking spectroscopy following the evolution of spectra on a single atomic location with temperature on an underdoped $Bi_2Sr_2CaCu_2O_{8+x}$ sample. The two energy scales in the spectra are marked by the arrows. (*b*) Normalized spectra measured on different underdoped samples showing the constancy of the low energy slope of the spectra (inset shows the region near zero bias). (*c*) Extraction of the gap as a function of angle following the model described in Reference 53. Adapted with permission from Reference 53, in which the details of the gap extraction from the spectra are explained in detail. (*d*) Schematic Fermi surface and gap evolution as a function of doping.

nodal region of the pairing gap and the observed quasilinear behavior follows the expected DOS of a *d*-wave superconductor. In this scenario, the slope of the spectra near E_F is directly related to the maximum of the *d*-wave gap; this is similar to the behavior observed in overdoped samples in which only one energy scale is seen in the spectra. In underdoped samples, the low energy slope of the STM spectra in the superconducting state no longer correlates with the behavior of the data at high bias. This anisotropic "two gap" scenario suggests that different portions of the Fermi surface are governed by either the pseudogap or the superconducting gap, and this hypothesis

can be used to model the shape of the spectra in underdoped samples. From this analysis, the pseudogap apparently shrinks the region of the Fermi surface over which a *d*-wave pairing gap can open. Remarkably, these measurements also show that the low bias spectra and associated near-nodal pairing gap are constant with doping below optimal doping. It follows that the reduction of T_c with underdoping occurs as the pseudogap limits the region of momentum space over which a *d*-wave superconducting gap can form (**Figure 7*c*,*d***). Recently these findings from STM studies have been corroborated by high-resolution ARPES studies that have made precise measurements of the near-nodal and antinodal gaps as a function of doping (54).

This dichotomy between antinodal and nodal regions of the Fermi surface in underdoped cuprates also plays a crucial role in the study of charge ordering in the cuprates. Combining measurements of the Fermi surface by ARPES with recent high energy-resolution QPI measurements of the $\mathbf{q}_1$ wave vector reveals that these modulations originate from the pseudogap state in the antinodal region. The momenta of these modulations track the band structure, starting at the antinode (small **q**) and terminate at the "hot spots" on the Fermi surface that separate the antinodal pseudogapped states from the nodal superconducting Fermi arcs. In contrast with the octet model, no modulations are observed with momenta connecting the nodal region (large **q**). Furthermore, tracking these modulations across T_c shows that the dispersing BdG quasiparticles that reside on the antinodal pseudogapped region below T_c transform into particle-hole asymmetric nondispersive modulations that are the signature of an ordering phenomenon above T_c. This is discussed in the next section.

4.3. Charge Order in the Cuprates

Charge ordering in the cuprates has been the subject of intense study starting with the discovery of charge and spin stripes near 1/8 doping in La-based cuprates (55). Since the first observation of real space modulations in the spectroscopic imaging of $Bi_2Sr_2CaCu_2O_{8+x}$, there have been claims that some of the observed spatial modulations were due to a charge ordering coexisting with the BdG-QPI features discussed in Section 4.2 (56–60). Important early evidence that there are two distinct phenomena responsible for the real space modulations at low energies came from STM studies of slightly overdoped samples, which revealed enhanced spatial modulations of the LDOS near vortex cores in the superconducting state and were interpreted as being the result of charge ordering in their immediate vicinity (56). Concurrent measurements on optimally doped $Bi_2Sr_2CaCu_2O_{8+x}$ samples in zero field also revealed static charge modulations (though these measurements were done below T_c, where dispersive BdG-QPI was expected) (58). Subsequent experiments on optimally doped $Bi_2Sr_2CaCu_2O_{8+x}$ that extended to temperatures above T_c (but below the pseudogap temperature T^*) showed that these nondispersing incommensurate modulations exist in the pseudogap phase and provided a stringent test for various ordering scenarios in the pseudogap of cuprates (21). Although separating QPI features from signatures of the CO has proven difficult in underdoped samples (59, 61, 62), these early results for samples near optimal doping suggested that the pseudogap phase is susceptible to the formation of short-ranged charge ordering.

The importance of incommensurate modulations in the SI-STM of underdoped samples at $T > T_c$ was reinforced by studies showing that they are first detected at T^* (61), providing evidence for an intimate connection between these modulations and the formation of the pseudogap. But the smoking gun came from high-resolution, temperature-dependent SI-STM measurements combined with bulk resonant X-ray scattering (RXS) that revealed the interplay between charge ordering and superconductivity and its distinction from BdG-QPI (63). Above T_c, an incommensurate charge modulation can be detected in both RXS and STM measurements of underdoped single- and double-layer Bi-based cuprates (**Figure 8**) (63, 64). In double-layer $Bi_2Sr_2CaCu_2O_{8+x}$

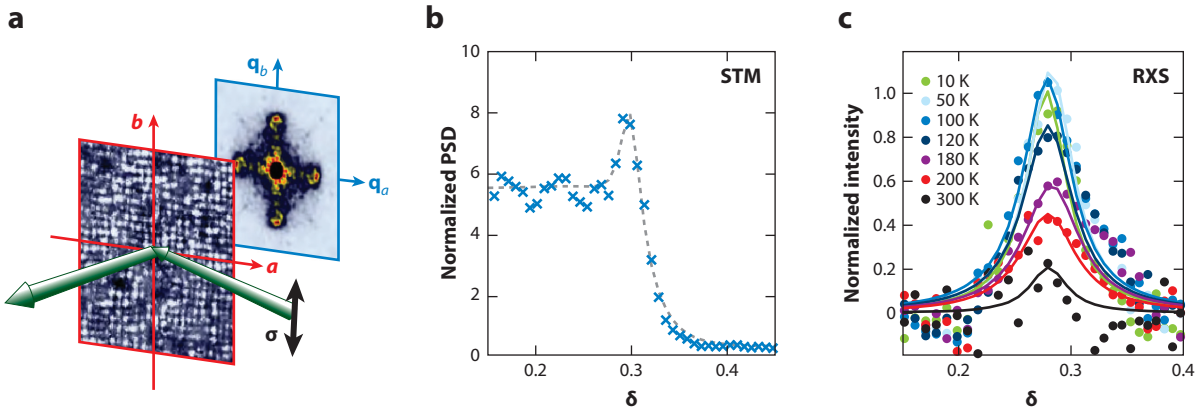

Figure 8

(*a*) Schematic of the combined experimental STM-RXS approach. RXS experiments were performed with vertically polarized photons (σ) in a horizontal scattering geometry and yielded momentum space information corresponding to the real space modulations seen by STM (charge ordering in the *front panel*) or, more directly, to the discrete Fourier transform of the STM real space data (*back panel*). (*b*) Line-cut of the energy-integrated (0 to 50 meV) discrete Fourier transform of an underdoped $Bi_2Sr_2CaCu_2O_{8+x}$ sample (T_c = 45 K) along the Cu-O bond direction showing a clear peak at $\delta = 0.30$ (where $\delta = 1$ represents the tetragonal Bragg peak). The CO peak appears at the same wave vector along the Cu-O bond direction in the Fourier transform of STM conductance maps and RXS studies as shown in panel *c* (after background subtraction at each temperature). Adapted with permission from Reference 63. Abbreviations: PSD, power spectral density; RXS, resonant X-ray scanning; STM, scanning tunneling microscope.

samples, approaching T_c from above, this modulation increases in intensity, reaching a maximum at T_c, and then becomes weaker inside the superconducting phase. Similar behavior with temperature had already been observed by means of X-ray studies on underdoped $YBa_2Cu_3O_{6+x}$ samples and interpreted as a signature of competition between charge ordering and superconductivity (65, 66). However, STM experiments were able to further provide important spectroscopic information about the nature of this competition. Above T_c, it was shown that the same CO observed by means of X-ray scattering occurs in an energy region between the Fermi energy and 50 meV, i.e., predominantly at positive bias and at lower energies than the pseudogap features. It was also shown that the appearance of superconductivity with the lowering of temperature gives rise to particle-hole symmetric dispersing BdG-QPI that grows in strength while the particle-hole asymmetric CO signature weakens (**Figure 9*a–d***) (63). Unlike the competition of charge ordering and superconductivity observed in conventional systems such as Nb_2Se_3, STM studies show that in the cuprates the same region of the Fermi surface participating in charge ordering eventually forms coherent superconducting quasiparticles. Combining the analysis of QPI at $T \ll T_c$ and Fermi surface information from ARPES, as well as model calculations, reveals that the electronic states most involved in this competition are those at the edge of pseudogap-induced Fermi arcs (**Figure 9*e***) (63, 64). This remarkable feature, together with the fact that incommensurate charge ordering can only be detected for positive bias, suggests that the charge order is different than typical charge density waves detected in other systems and likely related to the strong electron-electron correlations in the cuprates. These recent experiments together with scattering studies on other cuprates, provided evidence for the ubiquity of charge ordering in all underdoped hole-doped cuprates.

In concluding this section, we should add that evermore detailed STM studies of $Bi_2Sr_2CaCu_2O_{8+x}$ continue to be at the forefront of cuprate research. There are reports that STM data show evidence for C_4 symmetry breaking in these compounds (58, 59, 67–69). The SI-STM

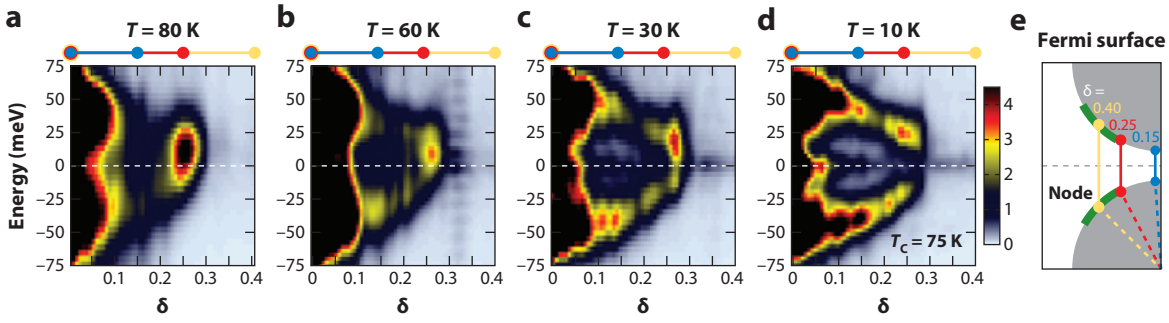

Figure 9

(*a–d*) Energy-momentum structure of the modulations seen in scanning tunneling microscopy along the Cu-O bond direction, extracted from discrete Fourier transforms for an underdoped $Bi_2Sr_2CaCu_2O_{8+x}$ sample measured at different temperatures. The data show the opposite temperature dependence between the particle-hole symmetric BdG-QPI and the particle-hole asymmetric charge ordering. (*e*) Schematic layout of the Fermi surface. The green segment represents the Fermi arc as determined by angle-resolved photoemission spectroscopy above T_c. The vertical lines (also reproduced horizontally at the tops of panels *a–d*) correspond to QPI wave vectors connecting the Fermi surface at different regions. Adapted with permission from Reference 63. Abbreviations: BdG, Bogoliubov-de Gennes; QPI, quasiparticle interference.

of the incommensurate CO wave vector discussed above reveals evidence for C_4 symmetry breaking by showing spatially alternating unidirectional domains for the CO (67, 70). These domains may represent a smectic phase that in the absence of any disorder would fully break C_4 symmetry and make one-dimensional stripe-like patterns. There have also been claims of intra-unit-cell nematicity from analysis of the STM conductance maps at the atomic modulation wavelength ($\mathbf{Q} = 0$) (68, 69). However, the analysis of such data (71) does not consider the experimental observation that different tip geometries can induce an energy-dependent C_4 symmetry breaking signal in C_4-symmetric materials (12). Recently, however, following RXS studies that determined the intra-unit-cell structure of the charge ordering in $YBa_2Cu_3O_{6+x}$ to be *d*-wave bond-ordered (72), a phase sensitive analysis of the CO modulations observed by STM has provided evidence that the CO is also of *d*-wave structure in $Bi_2Sr_2CaCu_2O_{8+x}$ (73).

5. SPECTROSCOPIC IMAGING OF HEAVY FERMIONS AND THEIR SUPERCONDUCTIVITY

In compounds with partially filled *f* orbitals, such as those containing lanthanide or actinides atoms, the interplay between local *f* electrons and those of more itinerant character give rise to a number of exotic electronic phenomena, such as the formation of heavy quasiparticles, as well as antiferromagnetism and unconventional superconductivity (74–76). Although these compounds have been the focus of many studies over the years, there is still much to be understood about the nature of their heavy quasiparticles, the highly interacting and potentially non-Fermi liquid phases they form, and the mechanism by which they become superconducting. Recently, SI-STM has had considerable success in the study of the formation of heavy-fermion states and their transformation into unconventional normal and superconducting states (77–82). The energy resolution of the STM provides a significant advantage over ARPES in both studying the formation of heavy quasiparticles—because of their narrow energy bandwidths—and probing the relatively small superconducting energy gap in these systems. In comparison with the cuprates, the SI-STM study of heavy fermions is more challenging not only because of the multiband character of their Fermi surfaces but because cleaved surfaces have different atomic terminations (77, 80). In particular,

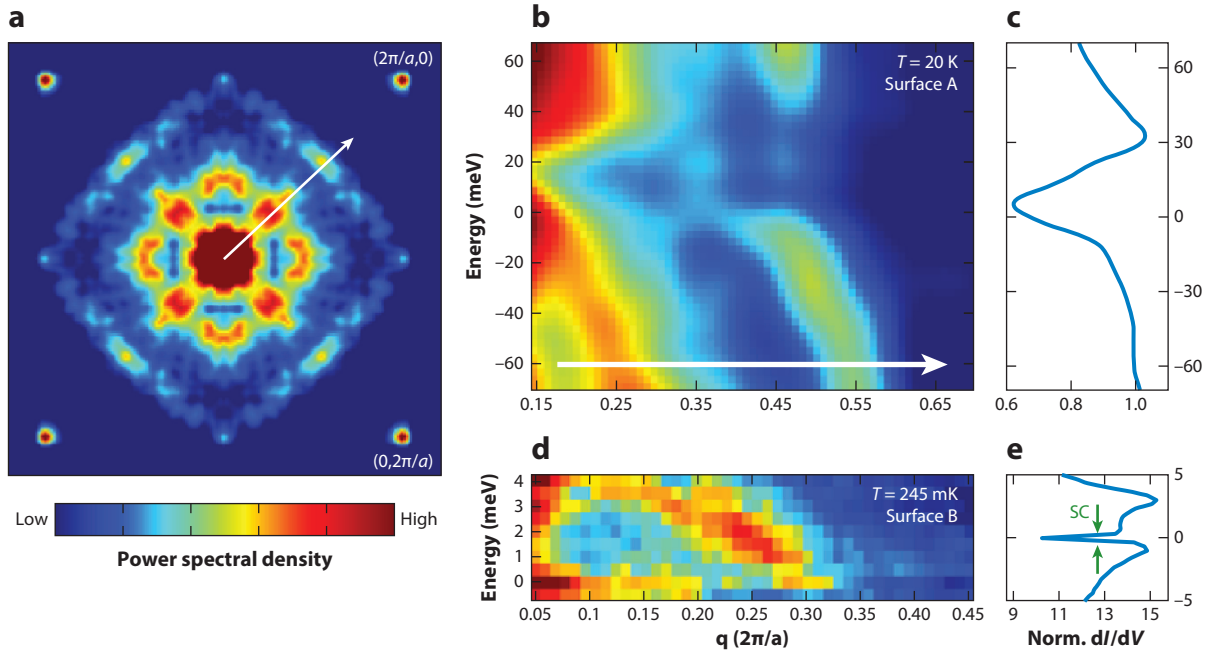

Figure 10

(*a*) QPI measurements on one of the surfaces (surface A, see Reference 80) of $CeCoIn_5$ measured above the superconducting transition temperature at −70 meV and 20 K. (*b*) Energy dependence of the QPI signal along (2π/*a*,0) on surface A (line in panel *a*) shows the presence of a heavy band near the Fermi level. The corresponding hybridization gap is shown in the spectra in panel *c*. (*d*) QPI signal on surface B (from reference 81), measured at 245 mK, and the corresponding spectra in panel *e* show how the spectra on this surface are sensitive to the heavy band with a peak in the density of states near the Fermi level. Abbreviation: QPI, quasiparticle interference.

several studies have now shown that the tunneling spectra can be drastically different depending on which surface termination is being probed. This surface dependence can be explained by different matrix elements for tunneling into different components (*f*- or *spd*-like) of the composite heavy quasiparticles that emerge in these materials. So far, experiments have been carried out on URu_2Si_2 (77, 78), $YbRu_2Si_2$ (79), and $CeCoIn_5$ (80–82). For these compounds and other heavy fermions, a prototypical maximum in the resistivity signals the temperature at which the *f*-electron behavior evolves from incoherent spin scattering of *spd*-like conduction electrons to that of a coherent band of heavy quasiparticles (76).

SI-STM measurements on $CeCoIn_5$ most clearly illustrate the process by which heavy quasiparticles form with reduced temperature (**Figure 10**) (80, 81). Although the band structure of this compound is complex and highly three-dimensional, SI-STM at high temperature shows distinct scattering wave vectors that disperse slowly with energy and characterize QPI from light bands (i.e., small effective mass). Upon cooling, in the region near the Fermi level, these slowly dispersive QPI peaks are significantly modified into rapidly dispersing wave vectors signaling the formation of heavy quasiparticles (**Figure 10*b*,*d***) (80, 81). These quasiparticles emerge at the edge of a hybridization gap that develops in these spectroscopic images (and associated spectra, **Figure 10*c*,*e***) in the same temperature range for which the resistivity indicates the formation of heavy-fermion coherence. The detailed signature of heavy-fermion formation in QPI and tunneling spectra is very sensitive to surface termination, which controls the matrix element for coupling to heavy or light components of the hybridized band structure (77, 80, 81, 83). As mentioned in Section 3

when discussing STM tunneling into single Kondo impurities, tunneling into a lattice of such impurities in the heavy-fermion compounds can also involve interference between different tunneling paths (84–86). Indeed, models that consider distinct tunneling processes and their interference into a hybridized band can be used to capture the detailed shape of the tunneling spectra on multiple surfaces of several heavy-fermion materials, including $YbRh_2Si_2$, $CeCoIn_5$, and URu_2Si_2 (77, 79, 80).

The heavy-fermion state is susceptible to strong correlation that often leads to the formation of exotic electronic states with the lowering of temperature. The URu_2Si_2 system is perhaps the most enigmatic example of such systems, which undergoes a second-order phase transition into the so-called hidden order phase below $T_{HO} = 17$ K (87, 88). To date, there is no clear understanding of the ordering phenomena that give rise to this phase transition and the underlying order parameter. STM measurements show that the heavy-fermion state that forms around 100 K in this compound undergoes dramatic changes at T_{HO} with the onset of the hidden order phase (77). The tunneling spectra show that a Fano line shape at high temperatures is modified by the development of electron-hole asymmetric gap below T_{HO}. This asymmetric gap increases in magnitude with the lowering of temperature similar to that of a mean-field order parameter (77). QPI measurements on this compound also show that this gap further modifies quasiparticle excitations in this system in a way that resembles a hybridization gap (78).

High-resolution studies of heavy-fermion superconductivity have also become possible with the development of new instruments that can reach ultralow temperatures, enabling high-resolution spectroscopy of the superconducting gap and low-energy BdG quasiparticle excitations in these compounds (89). Tunneling spectroscopy of $CeCoIn_5$ shows a *d*-wave-like gap with a rather high in-gap conductance developing below the superconducting transition temperature of this compound (**Figure 11*a*,*b***) (81, 82). Although QPI measurements show clear indications of BdG quasiparticles at $T < T_c$ or $H < H_{c2}$, they appear to coexist with particle-hole asymmetric excitations. Furthermore, the presence of multiple Fermi surface sheets makes it difficult to extract the underlying superconducting gap structure solely from the QPI measurements. Detailed modeling of the band structure and assumptions about the pairing gaps are therefore requisite to extract the gap symmetry from such STM measurements (90).

Atomic-scale imaging of impurities on the surface of cleaved $CeCoIn_5$ provides a spectacular demonstration of its nodal pairing character. The spatial structure of in-gap bound states, which are mixtures of electron-like and hole-like states, provides a direct probe of the order parameter symmetry (17, 33). Impurities that scatter electronic states in a manner consistent with the underlying crystalline symmetry in the normal state (at low T, $\mathbf{H} > \mathbf{H}_{c2}$) show in-gap bound states with a clover-leaf-shaped structure when $H < H_{c2}$ (**Figure 11*c*–*f***). The minima (maxima) in the oscillations for hole-like (electron-like) states identify the nodes of the *d*-wave order. By measuring the orientation of the nodes relative to the underlying lattice, it has been possible to directly show the d_{x2-y2} pairing symmetry of $CeCoIn_5$ (81).

Finally, STM studies of the temperature (and magnetic field) dependence of the superconducting gap in heavy fermions have shown parallels with those of underdoped cuprates. The superconducting state in the heavy-fermion systems emerges from a normal state at high temperature (or at high magnetic fields) that has a pseudogap in its low-energy excitations, (**Figure 11*b***) (81). Whether these low-energy states are characterized by broken symmetry remains to be uncovered.

6. OTHER CORRELATED MATERIALS

SI-STM is now being applied to a wide range of correlated materials, and there are many exciting experiments that have not been included in this short review. For example, experiments on lightly doped semiconductors have provided a new approach for studying electronic states

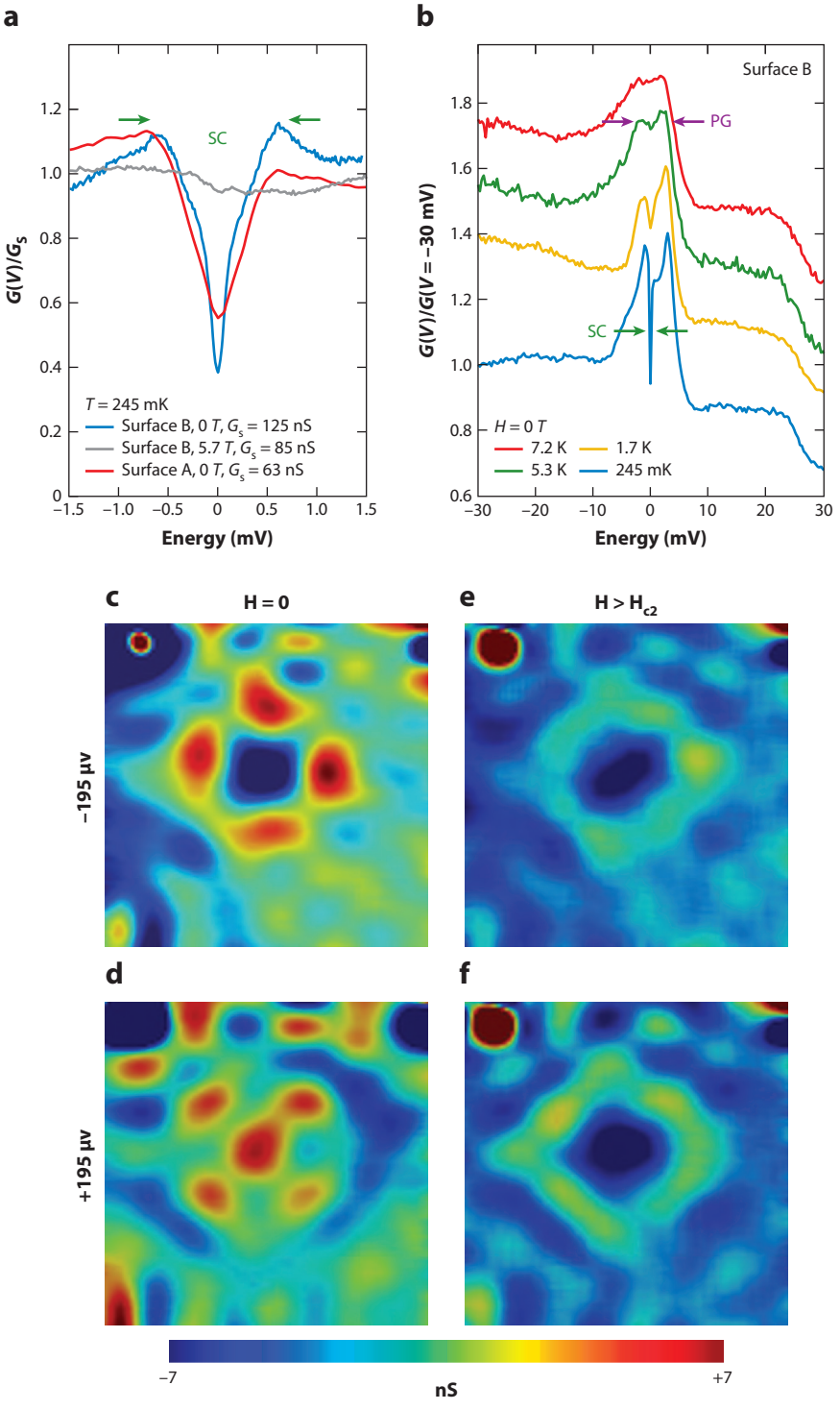

Figure 11

(*a*) Spectroscopic measurements in the normal and superconducting state of $CeCoIn_5$ measured on two different surfaces. (*b*) Spectroscopy on one of the surfaces (see Reference 81, labeled surface B here) is more sensitive to tunneling into the heavy band and shows a sharp peak near the Fermi energy. With decreasing temperature, the heavy band develops a pseudogap before the system undergoes transition into the superconducting state. (*c–f*) Electron and hole-like excitations near a single defect in the superconducting and normal states at low temperatures showing the local signature of pairing symmetry. The defect perturbs the normal state electron density in a manner consistent with the underlying crystal structure, whereas the superconducting state directly exhibits the anisotropic d_{x2-y2} pairing. Adapted with permission from Reference 81. Abbreviations: PG, pseudogap; SC, superconductivity.

on the verge of localization near the metal-insulator transition (91). In these disordered systems, STM experiments have provided evidence for critical phenomena and fractal wave functions in a regime where strong correlations are playing a dominant role. In the context of searching for interacting versions of topological insulators, there has been interest in examining the properties of Kondo insulator SmB_6, which shows a similar hybridization gap as the one discussed for the heavy-fermion compounds (92–93; also M.M. Yee, Y. Hee, A. Soumyanarayanan, D.-J. Kim, Z. Fisk, J.E. Hoffman, unpublished results, arXiv:1308.1085). There are also some recent examples of how dopants locally modify a Mott insulator in the very lightly doped regime for cuprates (70, 94) and other compounds (95–97) by examining the transformation of the Mott gap near individual defects. Finally, STM studies of Fe-based superconductors are increasingly contributing to the understanding of these materials and their unconventional superconductivity (97).

7. SUMMARY AND OUTLOOK

High-resolution SI-STM has emerged as a powerful tool in condensed matter physics with increasing applications to the study of novel and correlated electronic systems. Especially when combined with other spectroscopic and scattering tools, STM becomes a very powerful probe to provide energy-resolved information on the nature of quasiparticle states, their scattering, and the susceptibility of the electronic system to both short- and long-range ordering. The ability to combine such information with atomic-resolution images makes STM unique in many respects, providing information that cannot be obtained via any other technique. It is also worth noting that there are many technically feasible extensions of the STM that are yet to be developed or applied to correlated electronic systems. Spin-polarized STM, though now a powerful tool in the study of many metallic systems (98), has yet to be fully exploited for the study of correlated systems. Recent developments, such as combining spin polarized STM and atomic manipulation, have culminated in the ability to create artificial atomic structures for the realization of Majorana fermions (99) as well as potential toward atomic-scale logic circuits (100) and data storage (101). Although ultralow temperatures are now possible for many STM studies, operation in very high magnetic fields has yet to become a standard (89, 102). Landau-level spectroscopy with the STM is becoming an interesting method to probe the underlying electronic structure of materials. Similarly, whereas many studies of correlated systems have been performed on cleaved samples, the combination of molecular beam epitaxy and STM measurements have already begun to impact the field, as evidenced by the exciting work on topological insulators (103). As these several extensions mature, spectroscopic imaging with the STM will continue to play a central role in condensed matter physics.

DISCLOSURE STATEMENT

The authors are not aware of any affiliations, memberships, funding, or financial holdings that might be perceived as affecting the objectivity of this review.

ACKNOWLEDGMENTS

We are greatly indebted to our collaborators and colleagues over the years that have made it possible for us to explore many aspects of electronic phenomena in solids with the STM. In particular, we thank those who have been part of the research programs at the University of Illinois and Princeton University and have contributed to the results described in this review: Michael Vershinin, Shashank Misra, Dale Kitchen, Kenjiro Gomes, Abhay Pasupathy, Anthony Richardella, Aakash

Pushp, Lukas Urban, Pedram Roushan, Colin Parker, Haim Beidenkopf, Jungpil Seo, Brian Zhou, Andras Gyenis, Ilya Drozdov, and Stevan Nadj-Perge. Work at Princeton on the application of SI-STM to correlated electron systems is primarily supported by DOE-BES. The instrumentation and infrastructure at the Princeton Nanoscale Microscopy Laboratory used for many of the experiments described here were also supported by grants from NSF-DMR1104612, the NSF-MRSEC program through the Princeton Center for Complex Materials (DMR-0819860), the Wendy and Eric Schmidt Transformative Fund, and the W.M. Keck Foundation.

LITERATURE CITED

1. Giaever I. 1960. *Phys. Rev. Lett.* 5:147–48
2. McMillan WL, Rowell JM. 1965. *Phys. Rev. Lett.* 14:108
3. Binnig G, Rohrer H. 1987. *Rev. Mod. Phys.* 59:615–25
4. Crommie MF, Lutz CP, Eigler DM. 1993. *Science* 262:218–20
5. Fiete GA, Heller EJ. 2003. *Rev. Mod. Phys.* 75:933–48
6. Yazdani A, Jones BA, Lutz CP, Crommie MF, Eigler DM. 1997. *Science* 275:1767–70
7. Madhavan V, Chen W, Jamneala T, Crommie MF, Wingreen NS. 1998. *Science* 280:567–69
8. Petersen L, Sprunger PT, Hofmann P, Laegsgaard E, Briner BG, et al. 1998. *Phys. Rev. B* 57:R6858–61
9. Hoffman JE. 2011. *Rep. Progress Phys.* 74:124513
10. Bardeen J. 1961. *Phys. Rev. Lett.* 6:57
11. Tersoff J, Hamann DR. 1985. *Phys. Rev. B* 31:805–13
12. da Silva Neto EH, Aynajian P, Baumbach RE, Bauer ED, Mydosh J, et al. 2013. *Phys. Rev. B* 87:161117(R)
13. Wiesendanger R. 2009. *Rev. Mod. Phys.* 81:1495–56
14. Hewson AC. 1993. *The Kondo Problem to Heavy Fermions*. Cambridge, UK: Cambridge Press
15. Kouwenhoven L, Glazman L. 2001. *Phys. World* 14:33–38
16. Shiba H. 1968. *Progress Theor. Phys.* 40:435
17. Balatsky AV, Vekhter I, Zhu J-X. 2006. *Rev. Mod. Phys.* 78:373–433
18. Lee PA, Nagaosa N, Wen XG. 2006. *Rev. Mod. Phys.* 78:17–85
19. Scalapino DJ. 2012. *Rev. Mod. Phys.* 84:1383–417
20. Norman MR, Pines D, Kallin C. 2005. *Adv. Phys.* 54:715–33
21. Vershinin M, Misra S, Ono S, Abe Y, Ando Y, Yazdani A. 2004. *Science* 303:1995–98
22. Vojta M. 2009. *Adv. Phys.* 58:699–820
23. Fradkin E, Kivelson SA, Lawler MJ, Eisenstein JP, Mackenzie AP. 2010. *Annu. Rev. Condens. Matter Phys.* 1:153–78
24. Xu ZA, Ong NP, Wang Y, Kakeshita T, Uchida S. 2000. *Nature* 406:486–88
25. Fauqué B, Sidis Y, Hinkov V, Pailhès S, Lin CT, et al. 2006. *Phys. Rev. Lett.* 96:197001
26. Fischer O, Kugler M, Maggio-Aprile I, Berthod C, Renner C. 2007. *Rev. Mod. Phys.* 79:353–419
27. Damascelli A, Hussain Z, Shen Z-X. 2003. *Rev. Mod. Phys.* 75:473–541
28. Norman MR, Ding H, Randeria M, Campuzano JC, Yokoya T, et al. 1998. *Nature* 392:157–60
29. Yazdani A, Howald CM, Lutz CP, Kapitulnik A, Eigler DM. 1999. *Phys. Rev. Lett.* 83:176–79
30. Hudson EW, Pan SH, Gupta AK, Ng KW, Davis JC. 1999. *Science* 285:88–91
31. Pan SH, Hudson EW, Lang KM, Eisaki H, Uchida S, Davis JC. 2000. *Nature* 403:746–50
32. Hudson EW, Lang KM, Madhavan V, Pan SH, Eisaki H, et al. 2001. *Nature* 411:920–24
33. Haas S, Maki K. 2000. *Phys. Rev. Lett.* 85:2172–75
34. Misra S, Oh S, Hornbaker DJ, DiLuccio T, Eckstein JN, Yazdani A. 2002. *Phys. Rev. B* 66:100510
35. Howald C, Fournier R, Kapitulnik A. 2001. *Phys. Rev. B* 64:100504(R)
36. Pan SH, O'Neal JP, Badzey RL, Chamon C, Ding H, et al. 2001. *Nature* 413:282–85
37. Gomes K, Pasupathy A, Pushp A, Ono S, Ando Y, Yazdani A. 2007. *Nature* 447:569–72
38. Mcelroy K, Lee J, Slezak JA, Lee DH, Eisaki H, et al. 2005. *Science* 309:1048–52
39. Zeljkovic I, Xu ZJ, Wen JS, Gu GD, Markiewicz RS, Hoffman JE. 2012. *Science* 337:320–23
40. Pasupathy AN, Pushp A, Gomes KK, Parker CV, Wen J, et al. 2008. *Science* 320:196–201
41. Reber TJ, Plumb NC, Cao Y, Sun Z, Wang Q, et al. 2013. *Phys. Rev. B* 87:060506

42. Parker CV, Pushp A, Pasupathy AN, Gomes KK, Wen J, et al. 2010. *Phys. Rev. Lett.* 104:117001
43. Wang Y, Li L, Ong NP. 2006. *Phys. Rev. B* 73:024510
44. Dubroka A, Rössle M, Kim KW, Malik VK, Munzar D, et al. 2011. *Phys. Rev. Lett.* 106:047006
45. Wang Q-H, Lee D-H. 2003. *Phys. Rev. B* 67:020511(R)
46. Hoffman JE, McElroy K, Lee DH, Lang KM, Eisaki H, et al. 2002. *Science* 297:1148–51
47. McElroy K, Simmonds RW, Hoffman JE, Lee DH, Orenstein J, et al. 2003. *Nature* 422:592–96
48. Fujita K, Kim CK, Lee I, Lee J, Hamidian MH, et al. 2014. *Science* 344:612–16
49. He Y, Yin Y, Zech M, Soumyanarayanan A, Yee MM, et al. 2014. *Science* 344:608–11
50. Renner C, Revaz B, Genoud JY, Kadowaki K, Fischer O. 1998. *Phys. Rev. Lett.* 80:149–52
51. Boyer MC, Wise WD, Chatterjee K, Yi M, Kondo T, et al. 2007. *Nat. Phys.* 3:802–6
52. Alldredge JW, Lee J, McElroy K, Wang M, Fujita K, et al. 2008. *Nat. Phys.* 4:319–26
53. Pushp A, Parker CV, Pasupathy AN, Gomes KK, Ono S, et al. 2009. *Science* 324:1689–93
54. Vishik IM, Hashimoto M, He R-H, Lee W-S, Schmitt F, et al. 2012. *PNAS* 109:18332–37
55. Tranquada JM, Sternlieb BJ, Axe JD, Nakamura Y, Uchida S. 1995. *Nature* 375:561–63
56. Hoffman JE, Hudson EW, Lang KM, Madhavan V, Eisaki H, et al. 2002. *Science* 295:466–69
57. Howald C, Eisaki H, Kaneko N, Kapitulnik A. 2003. *PNAS* 100:9705–9
58. Howald C, Eisaki H, Kaneko N, Greven M, Kapitulnik A. 2003. *Phys. Rev. B* 67:014533
59. Kivelson SA, Bindloss IP, Fradkin E, Oganesyan V, Tranquada JM, et al. 2003. *Rev. Mod. Phys.* 75:1201
60. Wise WD. 2008. *Nat. Phys.* 4:696–99
61. Parker CV, Aynajian P, da Silva Neto EH, Pushp A, Ono S, et al. 2010. *Nature* 468:677–80
62. da Silva Neto EH, Parker CV, Aynajian P, Pushp A, Yazdani A, et al. 2012. *Phys. Rev. B* 85:104521
63. da Silva Neto EH, Aynajian P, Frano A, Comin R, Schierle E, et al. 2014. *Science* 343:393–96
64. Comin R, Frano A, Yee MM, Yoshida Y, Eisaki H, et al. 2014. *Science* 343:390–92
65. Ghiringhelli G, Le Tacon M, Minola M, Blanco-Canosa S, Mazzoli C, et al. 2012. *Science* 337:821–25
66. Chang J, Blackburn E, Holmes AT, Christensen NB, Larsen J, et al. 2012. *Nat. Phys.* 8:871–76
67. Kohsaka Y, Taylor C, Fujita K, Schmidt A, Lupien C, et al. 2007. *Science* 315:1380–85
68. Lawler MJ, Fujita K, Lee J, Schmidt AR, Kohsaka Y, et al. 2010. *Nature* 466:347–51
69. Mesaros A, Fujita K, Eisaki H, Uchida S, Davis JC, et al. 2011. *Science* 333:426–30
70. Kohsaka Y, Hanaguri T, Azuma M, Takano M, Davis JC, Takagi H. 2012. *Nat. Phys.* 8:534–38
71. Fujita K, Hamidian M, Firmo I, Mukhopadhyay S, Kim CK, et al. 2015. In *Strongly Correlated Systems*, Vol. 180, ed. A Avella, F Mancini, pp. 73–109. Berlin: Springer-Verlag
72. Comin R, Sutarto R, He F, da Silva Neto EH, Chauviere L, et al. 2015. *Nat. Mat.* 14:796–800
73. Fujita K, Hamidian MH, Edkins SD, Kim CK, Kohsaka Y, et al. 2014. *PNAS* 111:E3026–32
74. Stewart G. 1984. *Rev. Mod. Phys.* 56:755–87
75. Fisk Z, Sarrao JL, Smith JL, Thompson JD. 1995. *PNAS* 92:6663–67
76. Coleman P. 2007. In *Handbook of Magnetism and Advanced Magnetic Materials*, Vol. 1, *Fundamentals and Theory*, ed. H Kronmüller, S Parkin, pp. 95–148. New York: J. Wiley and Sons
77. Aynajian P, da Silva Neto EH, Parker CV, Huang Y, Pasupathy A, et al. 2010. *PNAS* 107:10383
78. Schmidt AR, Hamidian MH, Wahl P, Meier F, Balatsky AV, et al. 2010. *Nature* 465:570–76
79. Ernst S, Kirchner S, Krellner C, Geibel C, Zwicknagl G, et al. 2011. *Nature* 474:362–66
80. Aynajian P, da Silva Neto EH, Gyenis A, Baumbach RE, Thompson JD, et al. 2012. *Nature* 486:201–6
81. Zhou BB, Misra S, da Silva Neto EH, Aynajian P, Baumbach RE, et al. 2013. *Nat. Phys.* 9:474–79
82. Allan MP, Massee F, Morr DK, Van Dyke J, Rost AW, et al. 2013. *Nat. Phys.* 9:468–73
83. Aynajian P, da Silva Neto EH, Zhou BB, Misra S, Baumbach RE, et al. 2014. *J. Phys. Soc. Jpn.* 83:061008–18
84. Maltseva M, Dzero M, Coleman P. 2009. *Phys. Rev. Lett.* 103:206402
85. Figgins J, Morr DK. 2010. *Phys. Rev. Lett.* 104:187202
86. Benlagra A, Pruschke T, Vojta M. 2011. *Phys. Rev. B* 84:195141
87. Maple MB, Chen JW, Dalichaouch Y, Kohara T, Rossel C, et al. 1986. *Phys. Rev. Lett.* 56:185–88
88. Palstra TTM, Menovsky AA, Berg Jvd, Dirkmaat AJ, Kes PH, et al. 1985. *Phys. Rev. Lett.* 55:2727–30
89. Misra S, Zhou BB, Drozdov IK, Seo J, Urban L, et al. 2013. *Rev. Sci. Instrum.* 84:103903
90. Van Dyke JS, Massee F, Allan MP, Davis JCS, Petrovic C, Morr DK. 2014. *PNAS* 111:11663–67
91. Richardella A, Roushan P, Mack S, Zhou B, Huse DA, et al. 2010. *Science* 327:665–69

92. Ruan W, Ye C, Guo MH, Chen F, Chen XH, et al. 2014. *Phys. Rev. Lett.* 112:136401–6
93. Rossler S, Jang TH, Kim DJ, Tjeng LH, Fisk Z, et al. 2014. *PNAS* 111:4798–802
94. Ye C, Cai P, Yu RZ, Zhou XD, Ruan W, et al. 2013. *Nat. Commun.* 4:1365–71
95. Dhital C, Hogan T, Zhou W, Chen X, Ren Z, et al. 2014. *Nat. Commun.* 5:3377
96. Dai JX, Calleja E, Cao G, McElroy K. 2014. *Phys. Rev. B* 90:041102(R)
97. Song C-L, Hoffman JE. 2013. *Curr. Opin. Solid State Mater. Sci.* 17:39–48
98. Wiesendanger R. 2009. *Rev. Mod. Phys.* 81:1495–550
99. Nadj-Perge S, Drozdov IK, Li J, Chen H, Jeon S, et al. 2014. *Science* 346:602–7
100. Khajetoorians AA, Wiebe J, Chilian B, Wiesendanger R. 2011. *Science* 332:1062–64
101. Loth S, Baumann S, Lutz CP, Eigler DM, Heinrich AJ. 2012. *Science* 335:196–99
102. Song YJ, Otte AF, Shvarts V, Zhao ZY, Kuk Y, et al. 2010. *Rev. Sci. Instrum.* 81:121101
103. Beindenkopf H, Roushan P, Yazdani A. 2013. In *Contemporary Concepts of Condensed Matter Science*, Vol. 6, ed. M Franz, L Molenkamp, pp. 175–98. Amsterdam: Elsevier